Title

Molecular basis of RNase I-mediated rRNA degradation regulated by ribosomes

Authors

Atsushi Minami[1,†], Takehito Tanzawa[2,†,*], Tomoko Miyata[3,4], Fumiaki Makino[3,4,5], Zhuohao Yang[6], Takashi Funatsu[6], Tomohisa Kuzuyama[1,8], Hideji Yoshida[7], Takayuki Kato[2,9], Tetsuhiro Ogawa[1,8,*]

Affiliations

[1]Graduate School of Agricultural and Life Sciences, The University of Tokyo, Yayoi, Bunkyo-ku, Tokyo 113-8657, Japan.

[2]Institute for Protein Research, The University of Osaka, Suita, Osaka 565-0871, Japan.

[3]Graduate School of Frontier Biosciences, The University of Osaka, Yamadaoka, Suita, Osaka, 565-0871, Japan.

[4]JEOL YOKOGUSHI Research Alliance Laboratories, The University of Osaka, Yamadaoka, Suita, Osaka, 565-0871, Japan.

[5]JEOL Ltd, Musashino, Akishima, Tokyo, 196-8558, Japan.

[6]Graduate School of Pharmaceutical Sciences, The University of Tokyo, Bunkyo-ku, Tokyo 113-0033, Japan.

[7]Faculty of Medicine, Osaka Medical and Pharmaceutical University, Takatsuki, Osaka 569-0801, Japan.

[8]Collaborative Research Institute for Innovative Microbiology, The University of Tokyo, Yayoi, Bunkyo-ku, Tokyo 113-8657, Japan.

[9]Center for Advanced Modalities and DDS, The University of Osaka, Suita, Osaka 565-

0871, Japan

[†]These authors contributed equally to this work.

[*]Correspondence to:

Tetsuhiro Ogawa (atetsu@g.ecc.u-tokyo.ac.jp), Takehito Tanzawa

(takehito.tanzawa@protein.osaka-u.ac.jp).

Abstract

Protein biosynthesis is an energy-hungry intracellular process that requires the stringent regulation of ribosome abundance under environmental conditions. In response to stress, some active ribosomes are degraded while others, in bacteria, enter a hibernation state to protect against degradation. RNase I, a conserved T2 family ribonuclease in *Escherichia coli*, degrades ribosomal RNA to suppress biofilm formation, whereas it interacts with ribosomes. However, how and why RNase I binds to ribosomes remains elusive. Here, we show that hibernating ribosomes bind to RNase I and inhibit its activity, thereby promoting biofilm formation. We determined the cryo-electron microscopy structure of the hibernating ribosome complexed with RNase I. RNase I interacts with helix 41 of the 16S rRNA and the ribosomal protein uS14 in the head domain of the 30S subunit of the hibernating ribosome and positions its active centre away from helix 41, resulting in its catalytic inactivation. Hibernating ribosomes are protected from RNase I-mediated cleavage, and our *in vivo* and *in vitro* analyses revealed that RNase I targets dissociated large and small ribosomal subunits for rRNA degradation. These findings reveal a previously uncharacterized regulatory strategy that ribosomes modulate RNase I activity, ensuring both the preservation and timely degradation of ribosomes during environmental stress adaptation.

51 **Main**

52 Ribosomes are sophisticated molecular machines that translate genetic
53 information into proteins in all domains of life. Since protein biosynthesis consumes
54 substantial energy, cells tightly regulate ribosome abundance in response to
55 environmental conditions. In bacteria, under stress conditions such as nutrient starvation,
56 heat shock, oxidative stress, or entry into the stationary phase, ribosome biogenesis and
57 translation initiation are promptly suppressed[1], and excess active ribosomes are degraded[2].

58 Conversely, a subset of ribosomes is protected from degradation to ensure the
59 rapid resumption of translation once favourable conditions return. One strategy for
60 ribosome protection under stress is 'ribosome hibernation,' which preserves ribosomes in
61 a dormant state. This mechanism also prevents unnecessary translation for suppressing
62 energy consumption[3–6]. In many bacteria, ribosomes typically dimerize to form 100S
63 ribosomes with the involvement of ribosome-binding hibernation protein factors. Several
64 hibernation factors have been identified, including ribosome modulation factor (RMF),
65 hibernation-promoting factor (HPF), ribosome-associated inhibitor A (RaiA), and the
66 recently discovered Balon[3,7]. Ribosome hibernation is also reported in eukaryotes[8–11].

67 Ribonucleases (RNases) regulate cellular RNA metabolism by degrading
68 various types of RNA, including messenger RNA, transfer RNA, and ribosomal RNA.
69 The degradation of rRNA is essential for eliminating excess ribosomes. Among many
70 ribonucleases, RNase T2 is a crucial endoribonuclease that degrades rRNA in various
71 organisms[12–14] such as yeast RNase T2 (Rny1), which degrades rRNA during
72 autophagy[15,16]. RNase T2 was first discovered in *Aspergillus oryzae*[17] and later identified
73 in a wide range of organisms. It cleaves single-stranded RNA non-specifically using two
74 catalytic histidine residues[18]. The RNA cleavage mechanism consists of two steps: the

75 phosphodiester bond cleavage by phosphate transfer, which forms an intermediate 2′,3′-
76 cyclic nucleotide monophosphate (2′,3′-cNMPs), followed by hydrolysis to form the 3′-
77 phosphate group. However, in some cellular contexts, cyclic intermediates accumulate
78 because the second hydrolysis step is kinetically limited[19,20].

79 In contrast to RNase T2 in eukaryotes[12–14,21–23], little is known about its
80 biological functions in bacteria. *Escherichia coli* RNase T2, also called RNase I, is a
81 major ribonuclease that degrades rRNA, as in other species[24,25]. In addition, RNase I binds
82 to the ribosomal 30S subunit[26–28]. Although RNase I is predominantly localized in the
83 periplasm[26], these findings suggest that a fraction of RNase I resides and functions in the
84 cytoplasm. The molecular basis for this interaction and translocation remains unclear;
85 however, exposure to mercuric ions triggers extensive RNA degradation by RNase I in *E.*
86 *coli*, implying a role in stress-induced RNA decay[24]. Recently, it was shown that 2′,3′-
87 cNMPs, generated by RNase I, serve as second messengers and inhibit biofilm
88 formation[29]. Biofilms are aggregated communities of various microorganisms formed
89 under nutrient limitations and stress[30]. Thus, biofilm formation requires a reduction in
90 2′,3′-cNMP levels, i.e., to inhibit RNase I activity under such conditions. However, how
91 RNase I activity is regulated in response to environmental conditions remains unknown.

92 To investigate the underlying mechanisms of this regulation, we focused on the
93 interaction between RNase I and hibernating ribosomes, which accumulate under biofilm-
94 forming stress conditions. In this study, we demonstrate that RNase I activity is inhibited
95 by hibernating ribosomes both *in vitro* and *in vivo*, thereby promoting biofilm formation.
96 To understand the structural basis of this inhibition, we determined the cryo-EM structure
97 of the hibernating ribosome in complex with RNase I at a resolution of 2.7 Å. This
98 revealed that RNase I specifically binds to the head domain of the 30S subunit. Moreover,

99 our biochemical analyses explain the preferential association of RNase I with non-
100 translating ribosomes and reveal that ribosome dissociation into subunits exposes rRNAs
101 to cleavage by RNase I. Together, these findings elucidate the mechanism by which
102 ribosomes dynamically regulate their vulnerability to ribonuclease attacks, offering new
103 insights into the coevolution of ribosomes and RNA-degrading enzymes.
104

105 **RNase I-mediated rRNA degradation is suppressed in the *E. coli* strain**
106 **accumulating hibernating ribosomes**

107 In *E. coli*, a hibernating ribosome (100S ribosome) is formed by the dimerization
108 of two 70S ribosomes, and the formation is promoted by the binding of HPF and RMF.
109 The RaiA-deficient (Δ*raiA*) strain, lacking another hibernation factor RaiA, accumulates
110 100S ribosomes in the cytoplasm[31,32] (Supplementary Fig. 1a). We first compared rRNA
111 degradation among wild-type, RNase I-deficient (Δ*rna*), and Δ*raiA* strains under amino
112 acid starvation. After 2, 4, or 24 h of starvation, total RNA was extracted and analysed
113 by electrophoresis (Extended Data Fig. 1). At 2 h, rRNA degradation was largely
114 suppressed in both wild-type and Δ*raiA* strains. By 4 h, substantial rRNA degradation
115 occured in the wild-type strain, whereas rRNA was relatively preserved in the Δ*raiA*
116 strain. This was supported by quantitative analysis using a Bioanalyzer, which confirmed
117 that after 4 h of starvation, the wild-type strain retained 40% of 16S and 21% of 23S
118 rRNA, whereas the Δ*raiA* strain preserved 76% and 49%, respectively (Fig. 1a). These
119 results indicate that rRNA degradation is inhibited in the Δ*raiA* strain compared with that
120 in the wild-type strain. However, when cultivation under starvation was continued for up
121 to 24 h, extensive rRNA degradation occured in both strains, indicating that the protective
122 effect in the Δ*raiA* strain is not sustained under prolonged starvation (Extended Data Fig.

123 1). Almost no degradation was observed in the Δ*rna* strain even after 24 h of starvation,
124 confirming that RNase I is the primary ribonuclease responsible for rRNA degradation
125 during starvation (Fig. 1a and Extended Data Fig. 1).
126
127 **Inhibition of RNase I by hibernating ribosomes promotes biofilm formation**
128 Based on the above results, we next measured biofilm-forming ability. In the
129 Δ*raiA* and Δ*rna* strains, biofilm formation increased over 4-fold compared with that in
130 the wild-type strain (Fig. 1b, left panel). In the Δ*raiA* strain, biofilm levels decreased upon
131 RNase I overexpression (Fig. 1b, right panel), supporting our hypothesis that hibernating
132 ribosomes inhibit RNase I, leading to increased biofilm production in the Δ*raiA* strain.
133 To investigate how ribosome-associated RNase I activity is regulated, we examined its
134 interaction with hibernating ribosomes *in vivo*. Since most RNase I is localized in the
135 periplasm[26], we extracted spheroplasts to remove periplasmic RNase I and isolated
136 ribosomes from the resulting cytoplasmic lysate by ultrafiltration. Western blotting
137 showed that the ribosome fraction from the Δ*raiA* strain contained more RNase I than
138 that from the wild-type strain (Extended Data Fig. 2a). Further, higher RNase I activity
139 was detected in the ribosome fraction from the Δ*raiA* strain than the wild-type strain
140 (Extended Data Fig. 2b). These results suggest that hibernating ribosomes bind more
141 readily to RNase I than 70S ribosomes. Then, hibernating ribosomes were tested for their
142 ability to inhibit RNase I activity *in vitro*. Ribosomes were isolated from a Δ*rna* strain
143 accumulating 100S ribosomes (Δ*raiA*Δ*rna*) and from a strain lacking all hibernating
144 factors (Δ*raiA*Δ*hpf*Δ*rmf*Δ*rna*)[5] and incubated with RNase I. RNase I activity was
145 measured as described previously[28]. RNase I activity decreased in the presence of a higher
146 proportion of hibernating ribosomes (Fig. 1c), indicating that they inhibit RNase I activity.

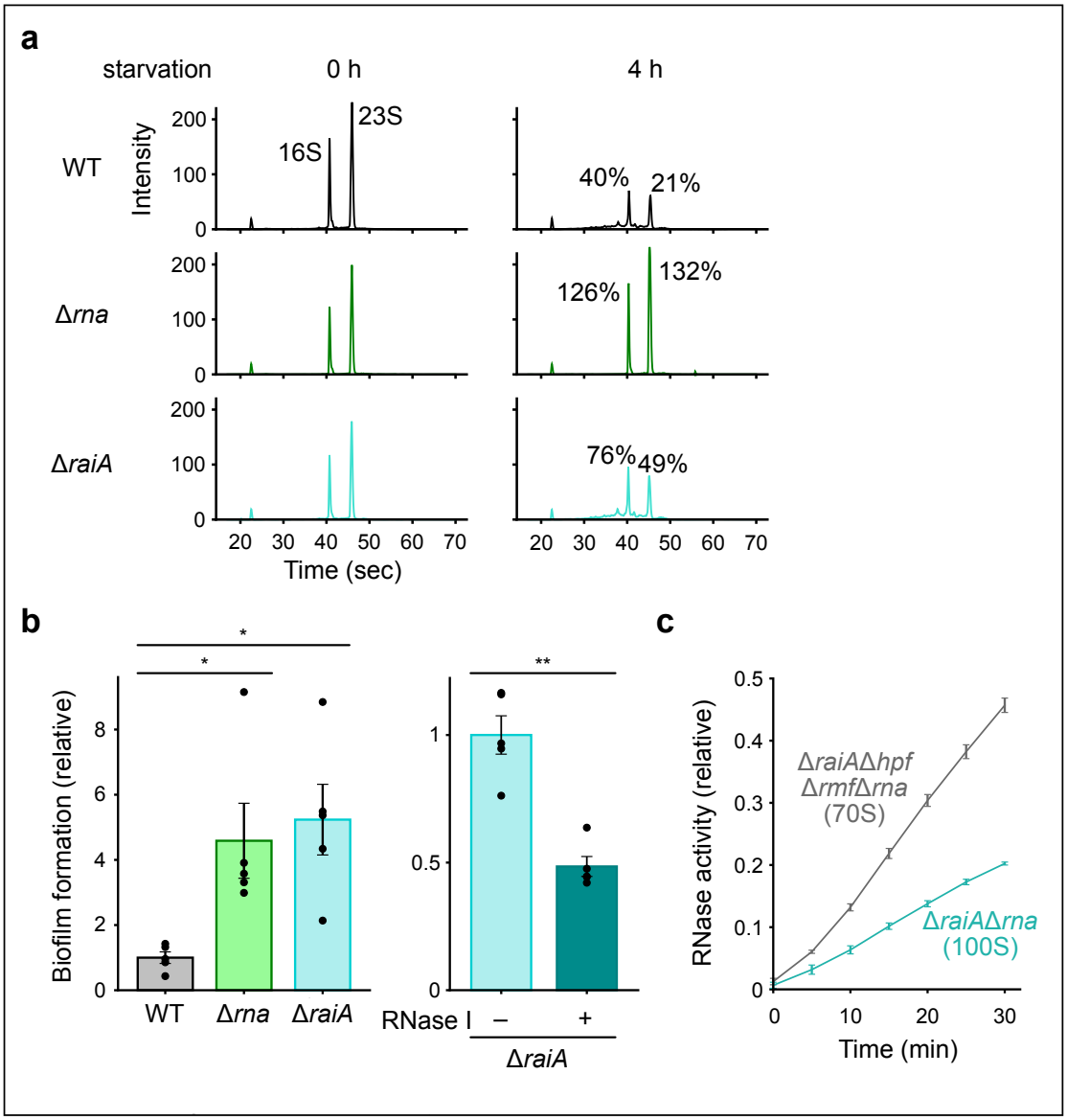

Fig. 1 | Suppression of RNase I-mediated rRNA degradation during starvation enhances biofilm formation in the Δ*raiA* strain.
a, Quantification of total RNAs prepared from wild-type (WT), Δ*rna,* and Δ*raiA* strains during amino acid starvation. Samples are arranged from top to bottom as WT, Δ*rna,* and Δ*raiA*, and from left to right as 0 h and 4 h after starvation. **b,** (left) Biofilm-forming ability of indicated strains during amino acid starvation. (right) Biofilm formation in the Δ*raiA* strain with or without RNase I overexpression. **c,** Comparison of the inhibitory activity of 70S ribosomes (from Δ*raiA*Δ*hpf*Δ*rmf*Δ*rna* cells) and 100S ribosomes (from Δ*raiA*Δ*rna* cells) against RNase I. Data in **b** and **c** represent mean ± standard error from five and three independent experiments, respectively. Asterisks indicate statistically significant differences (*P < 0.05, **P < 0.01; Welch's t-test).

160 **RNase I does not interact with translating ribosomes**

161 Our *in vivo* findings showed that hibernating ribosomes interact with RNase I
162 (Fig. 1c and Extended Data Fig. 2). To clarify whether this association is caused by the
163 direct interaction or is mediated indirectly by cellular co-factors, we reconstituted *in vitro*
164 hibernating ribosomes by adding RMF and HPF to 70S ribosomes (Supplementary Fig.
165 1b) and prepared a catalytically inactive mutant of RNase I (H55F/H133F) (hereafter,
166 'RNase I mutant'). The RNase I mutant bound to hibernating ribosomes in the absence of
167 additional factors, indicating that RNase I directly interacts with the ribosome (Fig. 2a).
168 In addition, the RNase I mutant bound almost equally well to both the 70S and hibernating
169 ribosomes. This result aligns with previous reports showing that RNase I associates with
170 ribosomes[26,27], and suggests that ribosome dimerization into the 100S form is not required
171 for RNase I binding. Moreover, it raised the possibility that RNase I binding depends on
172 the translational state of the ribosome rather than on its dimerization. RNase I bound less
173 efficiently to 70S ribosomes isolated from exponentially growing cells, where most
174 ribosomes are actively translating[33], than to ribosomes from hibernating state (Extended
175 Data Fig. 2). In the binding assay of RNase I in the presence or absence of *gfp* mRNA
176 using an *in vitro* translation system (PURE system) (Fig. 2b), RNase I binding was
177 markedly reduced when mRNA was added (Fig. 2c). A clear inverse correlation was
178 observed between mRNA concentration and RNase I binding: the higher the mRNA
179 concentration, the lower the level of RNase I binding, indicating that active translation
180 interferes with RNase I binding to ribosomes (Fig. 2d). In addition to the previous
181 studies[26,27], our experimental design enabled a direct comparison between translationally
182 active and inactive states and revealed that RNase I does not readily bind to ribosomes
183 during the translation process. Furthermore, this binding was restored upon addition of

184 RMF and HPF to ribosomes in the PURE system, which suppressed translation (Fig. 2e),
185 supporting our *in vivo* observation that RNase I interacts more strongly with hibernating
186 ribosomes than with ribosomes in the exponential phase (Fig. 1c and Extended Data Fig.
187 2). Together, these results provide a mechanistic link between RNase I suppression by
188 hibernating ribosomes and the enhanced biofilm-forming phenotype (Fig. 1a, b).
189

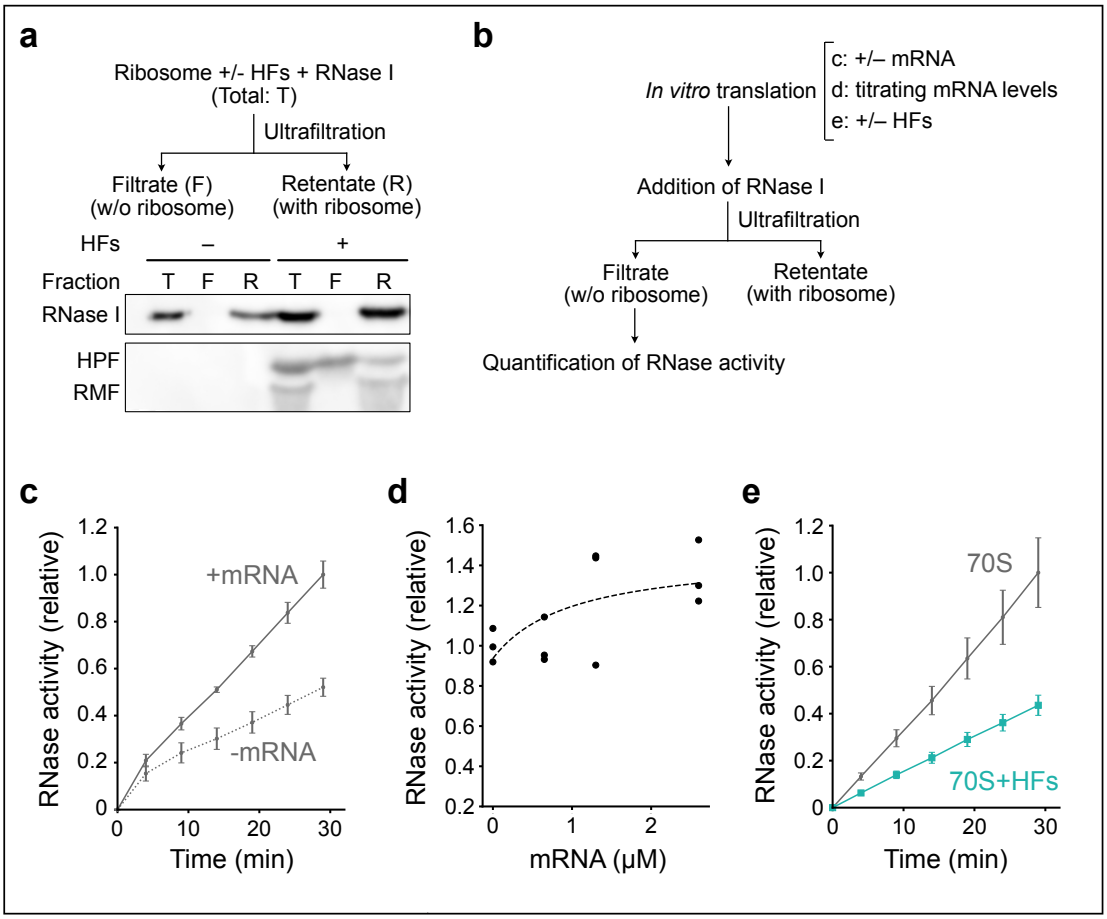

Fig. 2 | RNase I does not stably associate with translating 70S ribosomes. **a,** Binding ability of 70S ribosomes and *in vitro* reconstituted hibernating ribosomes to RNase I. 'T,' 'F,' and 'R' denote the total mixture, filtrate fraction, and retentate fraction, respectively. **b,** Schematic of the *in vitro* assay used to measure RNase I binding to ribosomes in the PURE system, corresponding to the experiments shown in **c-e**. **c,** RNase I binding with 70S ribosomes in the presence or absence of mRNA. **d,** RNase I binding with increasing mRNA concentrations. **e,** RNase I binding in the presence or absence of RMF and HPF (HFs).

200 **Structure of the hibernating ribosome bound to RNase I**

201 To elucidate how RNase I interacts with hibernating ribosomes, we reconstituted
202 a complex of the dimerized *E. coli* 100S ribosome and the RNase I mutant. The purified
203 RNase I mutant was mixed with 100S hibernating ribosomes isolated from *E. coli* W3110
204 cells in the stationary phase. The mixture was then applied to the EM-grids for cryo-EM
205 observations. We collected cryo-EM movies and performed single-particle analysis of the
206 100S•RNase I complex using two- and three-dimensional classifications (Extended Data
207 Fig. 3). Since the 100S ribosome easily dissociates into two 70S ribosome monomers at
208 low concentrations and tends to exhibit a preferred orientation on EM-grids[32,34], we
209 extracted 70S ribosome particles from the micrographs. The density map of the
210 70S•RNase I complex, in which both hibernation factors HPF and RMF were clearly
211 visible, was selected and refined. The resulting complex was obtained from 351,633
212 particles, yielding a density map at a resolution of 2.4 Å. However, because the density
213 of RMF was not fully occupied in this complex, the 3D classification was repeated to
214 enrich the density, finally yielding a refined map to a resolution of 2.7 Å consisting of
215 50,955 particles (Fig. 3a, Extended Data Table 1, and Extended Data Figs. 3 and 4a, b).

216 The structure of the RNase I mutant-bound hibernating complex revealed that
217 the RNase I mutant was bound to the head domain of the 30S subunit (Fig. 3a and
218 Extended Data Fig. 4c). As well as the structures of *E. coli* hibernation factors-bound
219 ribosome complex, the factors HPF and RMF interact with the mRNA channel between
220 the 30S head and body domains, and with the anti-Shine Dalgarno (anti-SD) region
221 between the 30S head and the platform binding centre (PBC), respectively[32,34,35].
222 Structural characterization further revealed that the C-terminal residues R69 and Y71 of
223 the ribosomal protein bS21 interacted with residues C1100 and A1167 of the 16S rRNA

224 near the PBC (Extended Data Fig. 5a). Compared with the previous structure (PDB
225 6H4N[32]), our structure shows subtle differences in the 30S subunit, which rotates
226 clockwise by ~1°, while the head domain swivels by ~2° (Supplementary Fig. 2). The
227 slight conformational changes caused by the RNase I mutant binding may contribute to
228 the structural arrangement of the PBC, promoting the stability of bS21 (Extended Data
229 Fig. 5a). In addition, the HPF stabilized the inter-subunit bridge B2a by changing the
230 conformation of the decoding centre and bridging to the 50S subunit (Extended Data Fig.
231 5b). Since the binding site of RNase I is located on the opposite side of the binding regions
232 for HPF and RMF, RNase I and the hibernation factors did not interfere with each other
233 (Fig. 3a). In addition, RNase I could be accommodated in the previous 100S ribosome
234 (PDB 6H58[32]) without steric clashes.

235 The overall shape of the RNase I mutant determined in this study is nearly
236 identical to the previous crystal structure (PDB 2Z70[36]). *E. coli* RNase I has a
237 characteristic arch-like architecture with active residues H55 and H133 and two piers. In
238 our complex structure, the piers of RNase I interact with the ribosome, and the active
239 centre remains over 6.5 Å from the ribosome, allowing 16S rRNA to evade cleavage (Fig.
240 3b). In addition to helix 41 (h41) of 16S rRNA, as indicated in a previous report[28], the
241 ribosomal protein uS14 interacts with the piers of the arch. Analysis of the binding
242 interfaces and areas using PDBe-PISA[37] and APBS[38] suggested that RNase I binds
243 primarily to h41 and secondarily to uS14, through shape complementarity (Fig. 3c,
244 Extended Data Fig. 6 and Extended Data Table 2).

245

246 **Interaction between the hibernating ribosome and RNase I**

247 The following details are provided regarding the structural basis for the

248 interaction of h41 and uS14 with RNase I. The h41 binds to RNase I by bridging the arch
249 piers (Fig. 3b and Extended Data Fig. 6a, b). The polar amino acid residues R31, R33,
250 Q198, and N233 of RNase I form hydrogen bonds with nucleotides G1272–A1274 in the
251 h41 stem region. Although these amino acids do not directly contact with the groove of
252 the h41 stem loop, they exploit the arch-shaped features of RNase I to interact with only
253 one strand of h41 (Fig. 3c and 3d [h-(i)]). In the other binding region, RNase I interacts
254 with A1257 and G1278 at the kink in the h41 stem. These two nucleotides are unpaired,
255 interacting with and stabilizing the binding of RNase I. In particular, the residue R83
256 forms hydrogen bonds with both A1257 and G1278 and exhibits stacking interactions
257 with the base of A1257 (Fig. 3c and 3d [h-(ii)]). Interestingly, upon RNase I binding, the
258 A1257 rotates approximately 100° towards the h41 stem-loop to avoid collision with R74
259 (Fig. 3e), indicating that the ribosome adapts its structure to accommodate RNase I by
260 partially altering its native interactions[39]. This rearrangement creates a pseudo-major
261 groove comprising A1257–G1260 and A1274–G1278, into which helix α4 of RNase I
262 fits via shape complementarity (Fig. 3d [h-(ii)] and Extended Data Fig. 7). In this structure,
263 F78 forms a π-stacking interaction with the base of A1257 on the opposite side of R83,
264 while R73 and R74 from helix α4 form hydrogen bonds with the ribose of A1257 (Fig.
265 3d [h-(ii)]). The conformational change of A1257 induced by RNase I binding disrupts
266 its native interaction with and F21 of uS14 (Fig. 3e), creating a cleft between h41 and
267 uS14 is filled by R74 of RNase I (Fig. 3d [s-(i)]). Instead of binding to A1257, R74 of
268 helix α4 binds to F21. Additionally, the loop containing G69–D71 of RNase I contacts
269 residues D18–A22 in the bent region of the N-terminal helix of uS14 (Fig. 3b and 3d [s-
270 (i)]). According to PDBe-PISA analysis, the N-terminal helix of uS14 also binds to the
271 RNase I by bridging both arch piers (Extended Data Fig. 6a, c). Residues P229–P231 in

272 the proline/glycine-rich long loop between β5 and β6 of RNase I form electrostatic
273 interactions with residues I30–N35 of uS14, including a hydrogen bond between H230
274 and D33 (Fig. 3c, 3d [s-(ii)]). Together, these findings provide structural insights into
275 how hibernating ribosomes associate with RNase I in a novel fashion that suppresses its
276 catalytic activity, thereby protecting themselves from degradation.
277

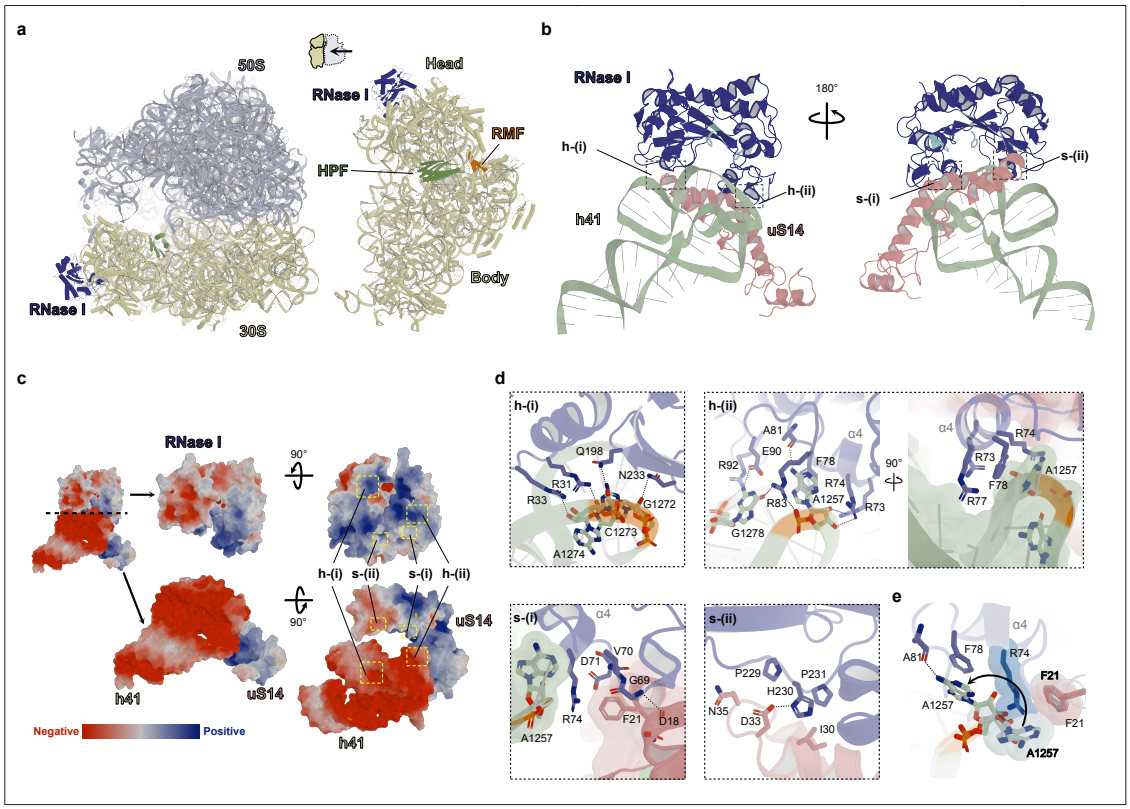

Fig. 3 | Structure of the RNase I-bound hibernating ribosome complex. **a,** Overall view of the RNase I-bound hibernating ribosome, showing the structure of the *E. coli* 70S ribosome (50S: light blue, 30S: light yellow) complexed with RNase I (dark blue), HPF (green), and RMF (orange) (left). A view of **a** from a different angle with the 50S subunit omitted for clarity (right). **b,** Close-up views of the interaction between RNase I and h41 (light green) of the 16S rRNA or the ribosomal protein uS14 (light pink) from two different angles. The active centre of RNase I is represented by stick models with pale blue. The h41 binding site is shown in h-(i) and h-(ii), and the uS14 binding site is shown in s-(i) and s-(ii). **c,** The electrostatic potential surface is shown in the same direction as **b**. Positive, negative, and neutral potentials are shown in blue, red, and white, respectively. Each binding site is illustrated by a yellow-dashed rectangle. **d,** Detailed views of the binding sites of RNase I on h41 and uS14. The amino acids and nucleotides involved in these bindings are represented by stick models, and the N, O, and P-atom are coloured blue, red, and orange, respectively. For easier understanding of the interactions, transparent surfaces are overlaid on the ribbon and stick models (h-(ii), s-(i)). The hydrogen bonds are indicated using dashed lines. **e,** Structural comparison of A1257 of h41 and F21 of uS14 between our model and a 70S ribosome (PDB 8SYL). The 8SYL ribosome is coloured whitish blue. Transparent surfaces are overlaid on stick models of the base of A1257 (8SYL), side chains of R74 (RNase I) and F21 (our model and 8SYL). The conformational

300 change in A1257 is indicated using a curved arrow.

301 **RNase I targets dissociated ribosomal subunits**

302 Although RNase I is inhibited on hibernating ribosomes, how RNase I targets
303 and degrades rRNA remains unclear. The association of ribosomal subunits provides
304 protection against RNases, as rRNA is shielded by ribosomal proteins[40]. Consistent with
305 this, we observed that RNase I hardly degrades rRNA within 70S ribosomes *in vitro*
306 (Extended Data Fig. 8a). Since ribosomes are estimated to outnumber RNase I by
307 approximately 100-fold in *E. coli* cells[28], the observation that a three-fold excess of RNase
308 I is required to degrade 70S ribosomes *in vitro* suggests that such degradation is unlikely
309 to occur under physiological conditions (Extended Data Fig. 8a). This implies that RNase
310 I preferentially cleaves rRNA within dissociated 30S and 50S subunits, rather than intact
311 70S ribosomes (Fig. 4a). Several rRNA fragments were observed, suggesting the presence
312 of specific RNase I cleavage sites at subunit interfaces. Notably, this degradation occurred
313 at equimolar concentrations of RNase I and ribosomes, in contrast to the degradation of
314 70S ribosomes (Fig. 4a and Extended Data Fig. 8a). Although dissociated subunits are
315 relatively scarce in exponentially growing cells, they transiently appear and are highly
316 susceptible to RNase I-mediated degradation, making them likely targets before assembly
317 into 70S ribosomes. Furthermore, as mentioned above, hibernating ribosomes are less
318 prone to dissociate into subunits. This feature aligns with the observed decrease in 2′,3′-
319 cNMP levels during the stationary phase[29], when hibernating ribosomes accumulate. To
320 confirm *in vivo* that subunit dissociation alters the susceptibility of rRNA to RNase I
321 cleavage, we treated *E. coli* cells with puromycin, which facilitates the release of nascent
322 polypeptides and promotes ribosome dissociation into subunits[41]. We then extracted 2′,3′-
323 cNMPs from the cells and analysed them by liquid chromatography–mass spectrometry
324 (LC–MS). Accumulation of dissociated subunits by the addition of puromycin led to

325 increased 2′,3′-cAMP and 2′,3′-cGMP levels in RNase I-expressing cells, indicating
326 enhanced rRNA degradation following subunit dissociation (Fig. 4b). Although 2′,3′-
327 cCMP and 2′,3′-cUMP levels also increased in puromycin-treated RNase I-expressing
328 cells, their levels were lower (Extended Data Fig. 8b). To summarize the above, RNase I
329 degrades rRNA within dissociated subunits and generates 2′,3′-cNMPs in the exponential
330 phase, contributing to the suppression of biofilm formation. We also detected 2′,3′-
331 cNMPs in puromycin-untreated cells, albeit at lower levels. This is consistent with a
332 previous study showing the presence of 2′,3′-cNMPs during the exponential phase[29].
333

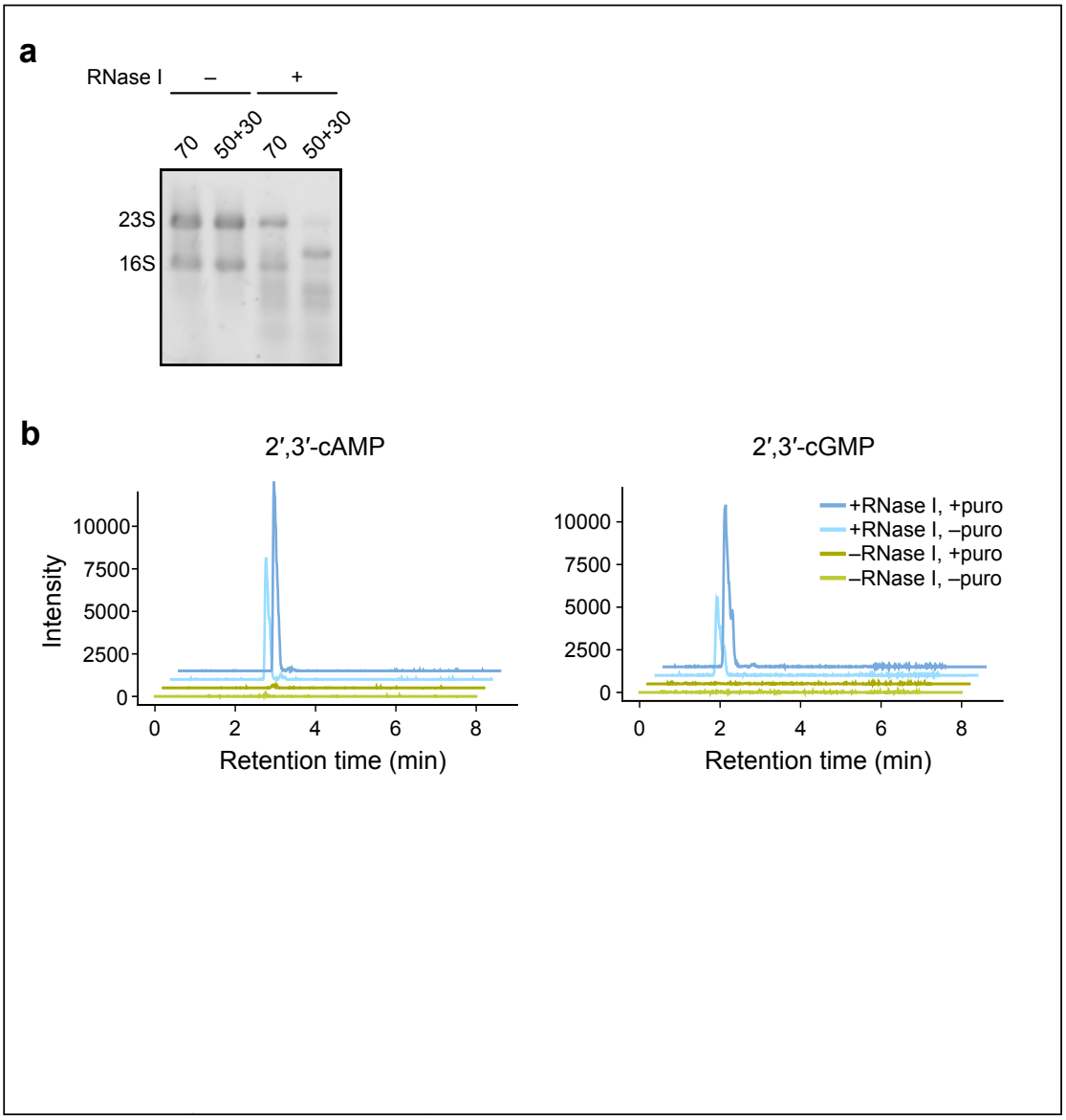

Fig. 4 | RNase I degrades rRNA from dissociated subunits.
a, Comparison of rRNA cleavage efficiency of RNase I between intact 70S ribosomes and dissociated 50S and 30S subunits. '70' indicates rRNAs from intact 70S ribosomes, whereas '50+30' indicates rRNAs from dissociated subunits. **b,** RNase I-mediated RNA cleavage in cells upon ribosome dissociation. Δ*rna* cells carrying either an empty vector or a plasmid expressing RNase I were treated with or without puromycin (puro), and the peaks of 2′,3′-cAMP and 2′,3′-cGMP in cell extracts were detected by LC–MS. Extracted ion chromatograms for 2′,3′-cAMP (upper; *m/z* 330.0598 $[M+H]^+$) and for 2′,3′-cGMP (lower; *m/z* 346.0547 $[M+H]^+$) are shown.

345 **Discussion**

346 Our study demonstrated that hibernating ribosomes suppress RNase I activity by
347 sequestering it in the head domain of the 30S subunit, thereby inhibiting rRNA cleavage
348 and promoting biofilm formation. These findings revealed that RNase I activity is
349 passively regulated by the ribosomal state; it is not accessible to actively translating
350 ribosomes, and is sequestered by hibernating ones. In addition, this study provides
351 mechanistic and structural insights into how RNase I binds to the 30S subunit of the
352 hibernating ribosome[26,27]. Although the ribosome protects itself from RNase I-mediated
353 cleavage, it is eventually degraded[31], consistent with our observation that RNase I
354 gradually degrades rRNA in hibernating ribosomes during prolonged stress (Extended
355 Data Fig. 1). Dimeric 100S ribosomes progressively dissociate during prolonged stress,
356 finally exposing their subunits[31]. Our study highlights the potential physiological role of
357 RNase I in binding to hibernating ribosomes. RNase I may not only lose catalytic activity
358 upon binding to hibernating ribosomes but also remain nearby, poised for rapid
359 degradation of ribosomes when required. This is consistent with a previous report
360 suggesting that rRNA degradation contributes to the recycling of phosphates and
361 nucleotides during starvation[42]. Furthermore, RNase I cleaves of rRNAs within
362 dissociated ribosomal subunits into fragments (Fig. 4a), which are then likely processed
363 by exoribonucleases such as RNase R or PNPase[40], and/or by RNase I itself, thereby
364 contributing to the clearance of excess ribosomes and adaptation to prolonged stress. This
365 degradation may also potentially serve as a programmed response facilitating the
366 transition to cell death when recovery is not possible. Conversely, upon recovery from
367 stress, the increase in 2′,3′-cNMP levels through ribosome degradation may promote
368 biofilm disassembly, allowing cells to prepare for regrowth.

369 Ribosome dissociation occurs naturally during the translation cycle via the
370 ribosome recycling factor, and accidentally stalled ribosomes on mRNA, on the other
371 hand, are rescued and split by ribosome rescue systems[43–45]. The conserved GTPase HflX
372 also functions as a ribosome-splitting factor for mRNA-vacant ribosomes[46]. Given that
373 RNase I efficiently cleaves rRNA in dissociated subunits (Fig. 4a, b) and the estimated
374 excess of ribosomes over RNase I molecules within the cell[28], targeting these fleeting
375 subunits rather than stable 70S complexes provides an efficient surveillance mechanism.
376 This model could directly link ribosomal conformational dynamics and quality-control
377 processes to rRNA degradation.

378 One of the most remarkable findings of this study is the elucidation of how
379 RNase I binds to the hibernating ribosome. Our structure reveals that the RNase I-binding
380 site lies within the 30S head domain, the conformation of which constantly fluctuates
381 during translation elongation because of swivel and rotation[47–49]. Such dynamic
382 fluctuations likely destabilize of the head domain during active translation[47], thereby
383 precluding its interaction with RNase I (Fig. 2c, d). In contrast, when ribosomes are not
384 actively engaged in translation or when ribosomes enter the hibernation state, the
385 fluctuation of the head domain is suppressed (Fig. 5 (i) and (ii)), facilitating stable RNase
386 I association. A molecular dynamics simulation of the translation initiation complex
387 predicted conformational fluctuations in the C1254–C1284 region of h41[49]. Notably, this
388 region includes A1257–G1260 and A1274–G1278, which interact directly with RNase I
389 in our structure (Fig. 3), suggesting that RNase I binding stabilizes these otherwise
390 dynamic regions of h41. This structural information raises the possibility that RNase I
391 binding suppresses the dynamics of the head domain and finally inhibits translation (Fig.
392 5(iv)). Consistent with this, RNase I inhibited protein synthesis *in vitro* in a concentration-

393 dependent manner (Extended Data Fig. 9). As the concentration of the RNase I mutant
394 increases, the binding–dissociation equilibrium may shift towards the bound state,
395 allowing RNase I to engage ribosomes in transiently non-translating states or promote
396 inactivation. Together, our structural and biochemical data highlight a bidirectional
397 relationship between ribosomal conformational states and RNase I activity.
398

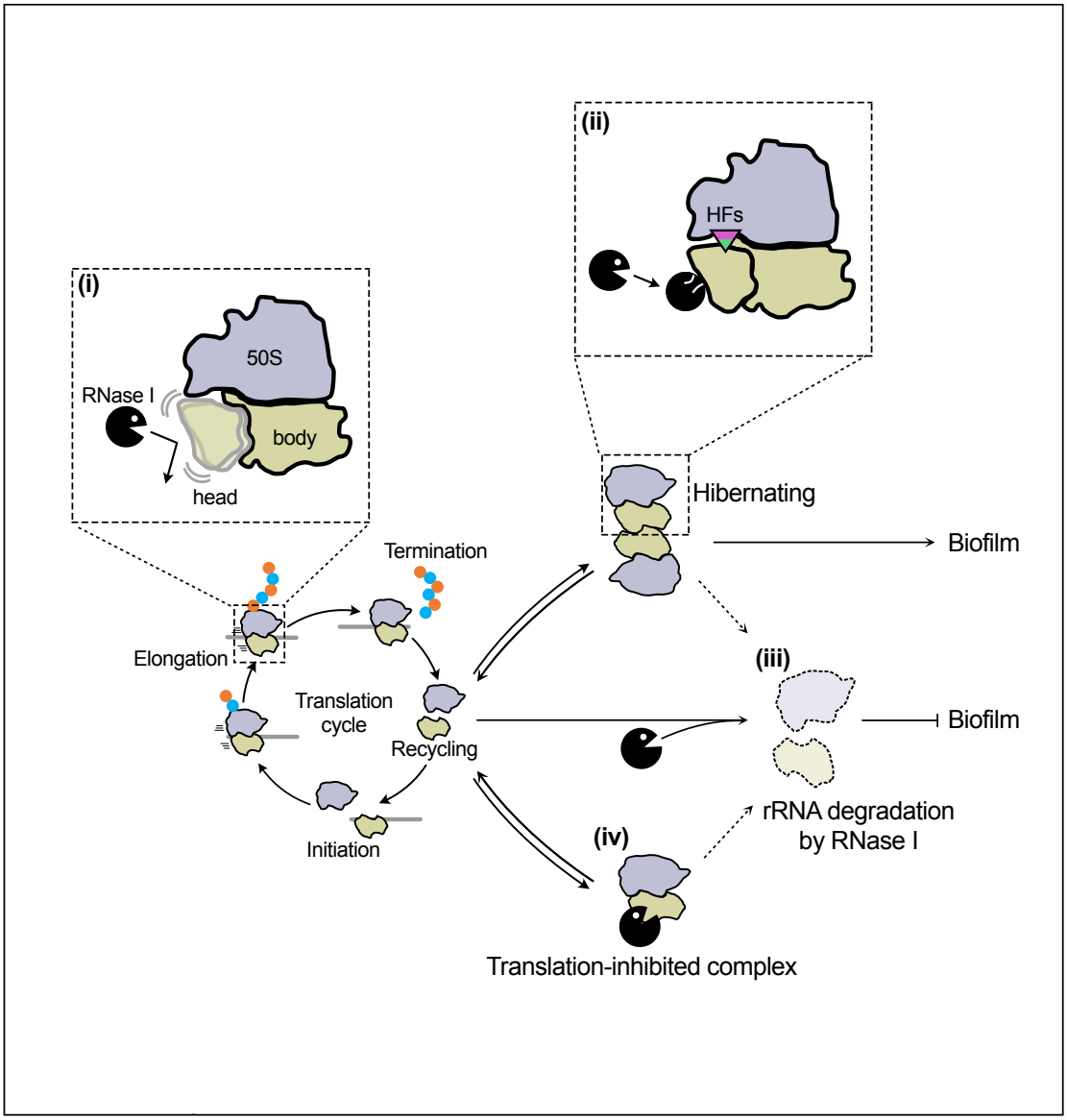

Fig. 5 | Regulation of RNase I by ribosomal states.
Schematic of the interaction between RNase I and ribosomes. (i) In the translating ribosome, the 30S head swivels relative to the body, rendering the RNase I binding site unstable and precluding productive engagement (related to Fig. 2b–d). (ii) Binding of HFs locks the head domain in a rigid conformation in the 100S complex, stabilizing RNase I binding (related to Figs. 1c, 2e, 3). (iii) Dissociated 30S and 50S subunits are recognized by RNase I and rRNAs are degraded (related to Fig. 4). (iv) The binding of RNase I to the non-translating 70S ribosome results in a translation-inhibited complex (related to Extended Data Fig. 9). Such complexes, as well as the hibernating ribosomes, may subsequently become targets for RNase I-mediated rRNA degradation if they dissociate into subunits.

412 Our cryo-EM structure shows that RNase I directly interacts with the ribosomal
413 protein uS14, providing new insight into the evolutionary plasticity of this conserved
414 ribosomal component. Although the gene encoding uS14 is essential[50], its precise role in
415 translation remains poorly understood. uS14 proteins are categorized into three classes
416 based on the presence or absence of a zinc-binding motif: C+, C– short, and C– long[51].
417 Compared with *Thermus thermophilus* uS14 (C+ class) in the crystal structure of the 70S
418 ribosome (PDB 4V8H[34]), *E. coli* uS14 (C– long class) possesses a distinct domain
419 insertion that forms the RNase I binding interface (Extended Data Fig. 10a). No RNase I
420 homologue was identified in *T. thermophilus*, suggesting that the interaction between
421 RNase I and uS14 may have evolved specifically in certain bacterial lineages.
422 Additionally, the presence of C+/– uS14 paralogue pairs in some bacteria, along with
423 reported differences in their functional properties[51–53], further supports the idea that uS14
424 is structurally adaptable, potentially enabling diverse functional acquisitions, including,
425 in *E. coli*, facilitating interaction with RNase I.

426 The binding interface between uS14 and RNase I raises the question of whether
427 the interaction depends solely on ribosomal features or also on structural adaptations in
428 RNase I. Structural comparison of *E. coli* RNase I and human RNase T2 revealed that *E.*
429 *coli* RNase I contains an internal insertion region (Extended Data Fig. 10b). This insertion
430 (S64–F78) forms a small domain of two short helices and connecting loops, which
431 contributes to the binding interface with both uS14 and h41 (Fig. 3d [s-(i)] and [h-(ii)],
432 Extended Data Figs. 6, 10b), suggesting that the ribosome-binding specificity of RNase I
433 is an evolutionary acquisition, likely shaped by coevolution with ribosomal elements such
434 as uS14 and h41. Although the overall structures of ribosomes are widely regarded as
435 highly conserved across species, local variations in rRNA and ribosomal protein

436 architecture have been known. Our findings suggest that ribosomes may have adapted
437 their structures not only for translation but also for interacting with regulatory factors like
438 RNase I.

439 Recently, cryo-EM structures of *Bacillus subtilis* RNase R in complex with the
440 30S subunit were determined, showing that it targets the anti-Shine-Dalgarno (anti-SD)
441 sequence and helix 44 within the decoding centre for rRNA degradation[54]. The RNase R
442 binding site overlaps with that of RMF (Extended Data Fig. 10c), indicating that RMF
443 functions as an inhibitor that protects hibernating ribosomes from RNase R-mediated
444 degradation[5]. Our structure represents an inactive state in which RNase I binds to the 30S
445 head domain in a manner that suppresses its catalytic activity. This interaction may allow
446 RNase I to remain poised for activation upon ribosome dissociation.

447 In summary, our findings provide insights into the mechanisms by which
448 ribosomes inhibit RNase I activity to preserve ribosome integrity under stress. This study
449 highlights ribosome–nuclease crosstalk, offering a novel perspective on how ribosomes
450 not only execute translation but also regulate RNA metabolism in response to
451 environmental stimuli.

452 **Methods**

453 ***Construction of strains and plasmids***

454 The strains and plasmids used in this study are listed in Supplementary Table S1.
455 RNase I, RaiA, RMF, or HPF-deficient strains (Δ*rna*, Δ*raiA*, Δ*rmf*, or Δ*hpf*, respectively)
456 were obtained from the Keio Collection, provided by the National BioResource Project-
457 E. coli (National Institute of Genetics, Japan)[55]. The kanamycin-resistance gene cassette
458 of the Keio Collection strains was removed by homologous recombination using plasmid
459 707-FLPe (Gene Bridges). Double (Δ*raiA*Δ*rna*) and quadruple knock-out strains
460 (Δ*raiA*Δ*hpf*Δ*rmf*Δ*rna*) were constructed by homologous recombination using the Red/ET
461 system (Gene Bridges).

462 The plasmid pET-*gfp* was constructed by inserting the *gfp* gene between the NcoI
463 and NotI sites of pET24d(+). The open reading frame (ORF) and promoter region of the
464 *rna* gene with a C-terminal FLAG tag were PCR-amplified and inserted into the pUC18
465 vector using the seamless cloning method (In-Fusion HD Cloning Kit, TaKaRa Bio). For
466 expression of His-tagged RNase I, RMF, and HPF, the respective ORFs were PCR-
467 amplified and inserted between the NcoI and EcoRI sites of pET24d(+). A plasmid
468 expressing a catalytically inactive RNase I mutant was constructed by substituting the
469 codons for H55 and H133 with phenylalanine in the *rna* gene on pET-*rna*.

470

471 ***Preparation of RNase I and hibernation factors***

472 *E. coli* BLR(DE3) strains transformed with plasmids expressing either His-
473 tagged RNase I, RMF, or HPF, were cultured in L-broth supplemented with 30 μg/mL
474 kanamycin. When an optical density at 660 nm (OD_{660}) reached 0.5, isopropyl β-D-1-
475 thiogalactopyranoside (IPTG) was added to the culture to a final concentration of 1 mM,

476 and the cells were further cultivated for 3 h at 37 °C. RNase I was purified as described
477 previously[16]. For the purification of RMF and HPF, buffer conditions were followed as
478 described in a previous publication[34]. For the purification of RMF, an equal volume of 2
479 M LiCl was added to the supernatant after sonication and stirred overnight at 4 °C,
480 followed by purification[56].
481
482 ***Isolation of ribosomes and sucrose density gradient centrifugation***
483 *E. coli* 70S ribosomes were prepared from the Δ*raiA*Δ*hpf*Δ*rmf*Δ*rna* strain as
484 described[57]. *E. coli* 100S ribosomes for cryo-EM were prepared as follows: 2 mL of an
485 overnight preculture of *E. coli* K-12 W3110 strain was obtained using medium E
486 (containing $MgSO_4$, citric acid, K_2HPO_4, and $NaNH_4HPO_4$) supplemented with 2%
487 polypeptone and 0.5% glucose[58]. Mass cultures were performed in 100 mL of the same
488 medium at 37 °C for 24 h. Cells were harvested and suspended in an association buffer
489 (20 mM Tris-HCl (pH 7.6), 15 mM $Mg(OAc)_2$, 100 mM NH_4OAc, and 6 mM β-
490 mercaptoethanol). Cells were vortexed with an approximately equal volume of glass
491 beads (212–300 μm, Merck KGaA) for 3 min. The homogenate was centrifuged at 12,000
492 × *g* for 8 min at 4 °C. The supernatant was applied on top of a 5–20% linear sucrose
493 density gradient in the association buffer and centrifuged using an SW 41 Ti rotor
494 (Beckman Coulter, Inc.) at 285,000 × *g* for 1.5 h at 4 °C. After centrifugation, the
495 absorbance was measured at 260 nm using a UV-1800 spectrophotometer (Shimadzu Co.)
496 to obtain ribosome profiles. The 100S ribosomal fractions were obtained based on the
497 profiles. The solution containing 100S ribosomes was concentrated, and sucrose was
498 removed using a centrifugal filter Amicon-100K (Merck KGaA).
499

500 ***Extraction of total RNA from E. coli cells***

501 *E. coli* strains were cultured in L-broth at 37 °C until an OD_{660} reached 0.5. Cells
502 were washed, suspended in M9 minimal medium (supplemented with 0.4% glucose and
503 0.2% casamino acids), and further incubated for 0, 2, 4, or 24 h. The cells were harvested
504 at the indicated time points, and total RNA was extracted using an RNeasy Mini Kit
505 (QIAGEN). Total RNA was analysed by electrophoresis on a denaturing 1% agarose gel
506 containing 2% formaldehyde in MOPS buffer or an Agilent 2100 Bioanalyzer (Agilent
507 Technologies).

508

509 ***Quantification of biofilm formation***

510 Biofilm formation was quantified by crystal violet staining following a published
511 procedure[59] with slight modifications as described[60]. *E. coli* was cultured in 10 mL of L-
512 broth at 37 °C to an OD_{660} of approximately 0.5. The culture was then diluted 1:100 in
513 M9 minimal medium with 0.2% casamino acids, and 100 µL aliquots were dispensed into
514 a U-bottom 96-well plate (FALCON #351177, Corning). The plates were incubated
515 statically at 30 °C for 24 h. Following incubation, non-adherent cells were decanted by
516 submerging the plates twice in a water bath. To stain the biofilm, 125 µL of 0.1% crystal
517 violet was added to each well and incubated at room temperature for 15 min on a rocking
518 shaker. Excess stain was removed by washing the plates twice in a water bath. The plates
519 were air-dried overnight. To solubilize the remaining crystal violet, 125 µL of 30% acetic
520 acid was added to each well, and the plate was shaken for 15 min. Absorbance was
521 measured at 570 nm using a microplate reader (Infinite F200, TECAN).

522

523 ***In vitro RNA degradation and RNase I binding assays***

524 RNA degradation assays were performed based on a previous study[28]. For the
525 inhibition assay (Fig. 1c), 0.075 pmol RNase I was incubated with 0.69 pmol of ribosomes.
526 Ribosomes were prepared from Δ*raiA*Δ*rna* or Δ*raiA*Δ*hpf*Δ*rmf*Δ*rna* strains following a
527 published method[31]. Mixtures were incubated at 30 °C for 30 min, and the activity of free
528 RNase I was quantified using the RNase Activity Assay Kit (Abcam).
529 For the binding assay (Extended Data Fig. 2), spheroplasts of *E. coli* cells were
530 prepared as follows: cells were washed with 10 mM Tris-HCl (pH 8.0), and the pellet was
531 suspended in 500 μL of the buffer containing 10 mM Tris-HCl (pH 8.0) and 0.5 M sucrose.
532 After 30 min of incubation, 500 μL of the buffer containing 10 mM Tris-HCl (pH 8.0)
533 and 2 mM EDTA was added, further incubated for 15 min, and centrifuged at 5,000 rpm
534 for 10 min. The pellet was suspended in 500 μL of water and centrifuged at 5,000 rpm
535 for 10 min. The lysate was loaded onto an ultrafiltration device (300,000 MWCO; PALL)
536 and centrifuged at 14,000 × *g*. After centrifugation, the retentate and filtrate were
537 separately collected. The amount of RNase I bound to ribosomes was detected by western
538 blotting or the RNase Activity Assay Kit.
539 The binding assay (Fig. 2a) was performed as follows: 20 μM of 70S ribosomes
540 were mixed with purified RMF and HPF (at least 10-fold molar excess over 70S
541 ribosomes) to reconstitute hibernating ribosomes *in vitro*. Thereafter, 20 μM of 70S
542 ribosomes or the reconstituted hibernating ribosomes were mixed with 120 μM of RNase
543 I mutant and incubated at 37 °C for 30 min. The mixture was then ultrafiltered at 14,000
544 × *g*, and the retentate and filtrate were collected separately. The RNase I mutant and
545 ribosomal protein (RpsB) in each sample were detected using western blotting. To detect
546 His-tagged RNase I, anti-6x histidine MoAb (9C11) (FUJIFILM Wako Pure Chemical
547 Corporation) and anti-mouse IgG, HRP-Linked Whole Ab Sheep (Cytiva) were used as

548 the primary and secondary antibodies, respectively. To detect RpsB, anti-rpsB antibody
549 (Abcam) and anti-rabbit IgG, HRP-Linked Whole Ab Sheep (Cytiva) were used.
550 The binding assay using *in vitro* translation (Fig. 2b–e) was performed as follows.
551 *In vitro* translation was performed in the presence or absence of *gfp* mRNA using
552 PURE*frex* 1.0 (GeneFrontier), the reconstituted translation system derived from *E. coli*[61].
553 The *gfp* mRNA was synthesized using the T7 RiboMAX Express Large Scale RNA
554 Production System (Promega), and transcripts were purified using NucleoSpin RNA
555 (MACHEREY-NAGEL). The translation mixture was incubated at 37 °C for 30 min.
556 RMF and HPF were added to ribosomes prior to initiating *in vitro* translation to
557 reconstitute hibernating ribosomes. RNase I mutant was added at a final concentration of
558 4.8 μM. After 30 min of further incubation, the reaction mixture was ultrafiltered, the
559 filtrate was collected, and the RNase I activity in the filtrate was measured as described
560 above.
561 For the *in vitro* translation inhibition assay (Extended Data Fig. 9), *in vitro*
562 translation was performed as described above with the following modifications: RNase I
563 mutant and 1 μM of ribosomes were added to the translation mixture and incubated for
564 30 min at 37 °C. Translation was initiated by adding *gfp* mRNA, and the translation
565 activity was evaluated based on GFP-derived fluorescence.
566
567 ***In vitro rRNA degradation from split ribosomal subunits***
568 The susceptibility of rRNA in 70S ribosomes, 30S, and 50S subunits to RNase I
569 was assessed as follows: 20 pmol of ribosomes were resuspended in the prokaryotic
570 ribosome dissociation buffer (10 mM Tris-HCl (pH 7.5), 1 mM $Mg(OAc)_2$, 100 mM
571 NH_4Cl, 1 mM DTT, 0.5 mM EDTA) and incubated overnight at 4 °C for 70S ribosome

572 dissociation[62]. Then RNase I (124 pmol) was added and incubated for 30 min at 37 °C.
573 Total rRNA was then extracted using RNeasy Mini Kit, as described above, and analysed
574 by electrophoresis on a denaturing agarose gel.
575
576 ***In vivo rRNA degradation from split ribosome subunits and detection of 2',3'-cNMPs***
577 ***using liquid chromatography–mass spectrometry (LC–MS)***
578 Ribosome dissociation *in vivo* was induced by puromycin treatment, based on
579 protocols modified from a previous research[41]. Δ*rna* strains harbouring either the empty
580 vector pUC18 or pUC18-*rna* were cultured in L-broth until an OD_{660} reached 0.5.
581 Puromycin was added to a final concentration of 100 μM, and cells were incubated for
582 15 min. Cyclic nucleotides were extracted as follows[63]: Cells were centrifuged at 10,000
583 rpm for 1 min, washed twice with sterile water, and resuspended in 1 mL of 1 M acetic
584 acid. After incubation on ice for 5 min, lysates were centrifuged at 15,000 rpm for 5 min.
585 Supernatants were collected, freeze-dried, resuspended in 100 μL of water, and filtered
586 using a Spin-X Centrifuge Tube Filter (Corning).
587 Liquid chromatography-electrospray ionization (ESI)-high-resolution mass
588 spectrometry (HRMS) analysis was performed using a SCIEX triple TOF X500R system
589 (SCIEX) equipped with an UFLC Nexera system (Shimadzu). The UFLC system was
590 equipped with a CAPCELLPAK C18 IF column (2.0 mm × 50 mm; Shiseido) and eluted
591 at a flow rate of 0.4 mL/min. The composition of mobile phase A was methanol–water
592 (3:97, v/v) and B was methanol–water (97:3, v/v), each containing 50 mM ammonium
593 acetate and 0.1% acetic acid[64]. The program was a linear gradient of 0–50% B for 5 min,
594 50–100% B for 1 min, 100% B for 3 min, 100–0% B for 1 min, and 0% B for 5 min. MS
595 and MS/MS parameters were as follows: ESI positive ion mode; acquisition mass range,

596 *m/z* 50–500; TOF accumulation time, 0.1 S; MS/MS accumulation time, 0.1 s; collision
597 energy, −10 eV; ion source gas 1, 60 psi; ion source gas 2, 60 psi; curtain gas 30 psi; ion
598 spray voltage floating, −4500 v; temperature 350 °C. MS data were analysed using an
599 Analyst software (SCIEX).
600
601 ***Sample preparation and cryo-electron microscopy data acquisition***
602 The ribosome•RNase I complex was reconstructed using 1.2 μM 100S
603 hibernating ribosomes containing HPF and RMF from *E. coli* K-12 W3110 strain and 7.2
604 μM RNase I in the reaction buffer (20 mM HEPES-KOH (pH 7.6), 10 mM $Mg(OAc)_2$,
605 30 mM NH_4Cl, and 6 mM β-mercaptoethanol) at 37 °C for 30 min. The complex was
606 diluted by 1.5-fold, applied onto an EM-grid, and plunge-frozen in liquid nitrogen-cooled
607 ethane. Quantifoil R2/2 gold 200 mesh grids (Quantifoil Micro Tools GmbH) glow-
608 discharged for 30 s in a PIB-10 Ion Bombarder (Vacuum Device Inc) were used to apply
609 2.7 μL sample, pre-incubated for 10 s, blotted for 15 s, and post-incubated for 2 s at 4 °C
610 and 100% humidity before freezing in a Vitrobot Mark IV (Thermo Fisher Scientific).
611 The grids were subsequently clipped into an autogrid cartridge and transferred into a
612 CRYO ARM™ 300 II field emission cryo-electron microscope (JEOL) operating at 300
613 keV. Data were acquired with a K3 camera (Gatan) using SerialEM software[65]. The cryo-
614 EM movies were acquired at a calibrated magnification of 80,460 and a pixel size of 0.87
615 Å/pixel to record movies with 70 frames with a total accumulated dose of 50 $e^-/Å^2$/movie.
616
617 ***Cryo-electron microscopy image processing***
618 All steps of the image processing were performed using cryoSPARC 3.3.1 and
619 4.0.0 software[66]. 2,000 of 33,302 movies were initially motion-corrected by the patch

620 motion correction job, followed by the patch CTF estimation. A total of 258,744 particles
621 were picked by circular blob (size 260–300 Å) using the blob picker job and extracted at
622 4-fold decimated pixel size (3.48 Å/pixel). The extracted particles were two-dimensional
623 (2D) classified to remove the classes of 30S subunits and debris. The 70S particles were
624 re-picked at a size of 360 Å using the classes selected as templates, followed by the
625 extraction from micrographs job and 2D classification jobs. Five ab-initio volumes were
626 reconstructed using selected 146,282 particles to obtain the main class average of the 70S
627 ribosome; the classes of 50S subunit and debris were discarded by heterogeneous
628 refinement. After the 70S-like particles were combined using homogeneous refinement,
629 followed by local refinement with signal subtraction on the 30S head, a three-dimensional
630 (3D) classification focused on the head region was performed to obtain RNase I-binding
631 particles. Selected 33,823 particles were extracted at 1.25-fold decimated pixel size
632 (2.175 Å/pixel), the complex could not find the RMF in the volume at a nominal
633 resolution of 2.7 Å. Remaining movies were processed in the same way as described
634 above. Heterogeneous refinement was performed to extract 70S-like classes composed of
635 total 1,501,256 particles from the 2D classes of all 33,294 micrographs. A soft mask
636 focused on the 30S head with hibernation factors and RNase I was generated using UCSF
637 ChimeraX 1.5[67], before 351,633 particles containing hibernating 70S with RNase I were
638 obtained by the 3D classification, followed by the local refinement with signal subtraction
639 to improve the local resolution of the focused region. Resulting the local 3D volume was
640 refined to a nominal resolution of 2.4 Å, yet the density of RMF remained poor. Two
641 rounds of 3D classification were performed, and particles containing the weak density
642 map of RMF were discarded. 3D classification using the mask on the 30S platform,
643 including S1, further sorted out 50,955 particles, including RMF and part of S1. The final

644 reconstruction was refined to a resolution of 2.7 Å in a homogeneous map and to 2.7 Å
645 in a local map of the mask on 30S head, taking into account the global/local CTF
646 refinements after the particles were re-extracted at 1.4-fold decimated pixel size (1.21 Å
647 per pixel). Since the orientation of both homogeneous and local volumes were slightly
648 different, the local volume was docked into the homogeneous volume using the 'Fit in
649 Map' function and resampled to the grid of homogeneous refinement using trilinear
650 interpolation by the 'volume resample' operation in ChimeraX 1.6.1[67].
651
652 ***Model building and refinement***
653 The structure of the *E. coli* 70S ribosome in this study was built in the 2.7 Å
654 density map obtained from homogeneous refinement in cryoSPARC, using a model of
655 the *E. coli* 70S ribosome structure (PDB 8SYL[5]) as a template. After removing all
656 molecules and ions other than ribosome components of the 8SYL model, the ribosomal
657 subunits, split into 50S and 30S using PyMOL, were docked as rigid bodies into the
658 density map using the 'Fit in Map' function in ChimeraX 1.6.1[67]. The model of each
659 subunit was refined with jelly-body restraints using Servalcat 0.4.74[68]. The models were
660 manually corrected for ribosomal proteins according to secondary structure and
661 Ramachandran restraints for better fitting into the density map using the 'Real Space
662 Refine Zone' function in Coot 0.9.8.95[69,70]. In addition, the nucleotides of the rRNA
663 chains in the models were manually corrected for syn- or anti-conformations with
664 reference to the differential Fourier map produced by Servalcat. The models of the HPF
665 derived from the crystal structure of *Tth*70S•*Eco*HPF complex (PDB 4V8H[34]) and the
666 RMF derived from the cryo-EM structure of *E. coli* hibernating ribosome complex (PDB
667 6H4N[70,71]) were rigid-body fitted into the homogenous density map. The crystal structure

668 of *Eco*RNase I (PDB 2Z70[36]) was rigid-body fitted into the EM density map of the local
669 refinement focused on the 30S head region in cryoSPARC; two mutated residues, H55F
670 and H133F, at the active site of the RNase I model were also manually modified and
671 corrected in Coot. These models were merged into the 30S model before it was jelly-body
672 refined by Servalcat, and the 30S binding partners, especially, were manually corrected
673 residue by residue in Coot, together with Ramachandran and secondary structure
674 restraints. After merging the models of the 30S and 50S complexes into the hibernating
675 70S•RNase I complex, a series of operations in jelly-body refinement and manual
676 correction were repeated several times until the model satisfied its geometry. Magnesium
677 ions and water molecules from 8SYL were docked into the model of the 70S•RNase I
678 complex in Coot. After refining the small molecules merged with the complex using
679 Servalcat, their atomic coordinates were manually corrected or removed to better fit the
680 density map and the differential Fourier map. The resulting model was validated using
681 the comprehensive validation tool for cryo-EM in PHENIX 1.21.1[71,72] (Extended Data
682 Table S1).
683
684 ***APBS and PISA calculations***
685 The surface potential values were produced using APBS[38]. The interfacing
686 residues and the buried surface areas were calculated using the protein interface, surfaces,
687 and assemblies (PISA) provided by Protein Data Bank Europe (PDBe)[37]
688 (https://www.ebi.ac.uk/pdbe/pisa/). Colour coding based on the BSA values was
689 performed on PyMOL using the original Python program colorByBSA.py
690 (https://github.com/minami1009/colorByBSA).
691

692 ***Preparation of figures***

693 Figures were generated using PyMOL (The PyMOL Molecular Graphics System,
694 Versions 3.0.0 and 3.1.0 Schrödinger, LLC), Chimera X 1.7.1, Matplotlib (Version 3.7.1),
695 and Seaborn (Version 0.13.1) libraries in Python (Version 3.10.12), OmniGraffle
696 (Version 7.18.6), and Affinity Designer (Version 1.10.5).

697

698 **Data availability**

699 The atomic coordinate of the hibernating 70S ribosome in complex with the
700 RNase I mutant was deposited in the Protein Data Bank Japan (PDBj) under accession
701 code 9IOT. The cryo-EM map was deposited in the Electron Microscopy Data Bank
702 (EMDB) under accession code EMD-60747, and the local map focused on the 30S head
703 was deposited as an additional map.

704

705 **Acknowledgments**

706 We thank MG. Gagnon and M. Yao for critical reading of the manuscript and
707 offering suggestions; T. Suzuki, A. Nagao and N. Akiyama for performing the SDGC and
708 isolating of ribosomes; members of the Synthetic Biology Laboratory and T. Shiraishi for
709 supporting and advising on LC-MS analysis; members of the T. Kato group and J.
710 Kishikawa for supporting and advising on the cryo-EM single particle analysis; K.
711 Yamashita for advising on model refinement using Servalcat; and Y. Maki for discussions.
712 We are also grateful to late T. Beppu for the discussion. This work was funded by JSPS
713 KAKENHI (Grant numbers JP20K21266 and JP23H02122) to T.O. and by JST SPRING
714 (Grant number JPMJSP2108) to A.M. The collection of EM movies for single particle
715 analysis was performed using the CRYO ARM 300 II at the JEOL YOKOGUSHI

Research Alliance Laboratories of the Graduate School of Frontier Biosciences, The University of Osaka. This research was supported by the Research Support Project for Life Science and Drug Discovery (Basis for Supporting Innovative Drug Discovery and Life Science Research (BINDS)) from AMED under Grant Number JP23ama121001.

Author contributions

A.M.: conceptualization, data curation, formal analysis, funding acquisition, investigation, methodology, software, visualization, writing - original draft, review and editing. T.T.: data curation, formal analysis, investigation, software, visualization, writing - original draft, review and editing. T.M.: investigation. F.M.: investigation. Z.Y.: methodology. T.F.: methodology, writing - review and editing. To.K.: supervision, writing - review and editing. H.Y.: investigation, resources, writing - review and editing. Ta.K.: funding acquisition, supervision, writing - review and editing. T.O.: conceptualization, data curation, methodology, funding acquisition, project administration, supervision, writing - original draft, review and editing.

Competing interests

The authors declare no competing interests.

Additional information

Supplementary Information is available for this paper.

Correspondence and requests for material should be addressed to Tetsuhiro Ogawa (atetsu@g.ecc.u-tokyo.ac.jp) or Takehito Tanzawa (takehito.tanzawa@protein.osaka-u.ac.jp).

740 **Reprints and permissions information** is available at www.nature.com/reprints.

741

742 **References**

743 1. Irving, S. E., Choudhury, N. R. & Corrigan, R. M. The stringent response and
744 physiological roles of (pp)pGpp in bacteria. *Nat. Rev. Microbiol.* **19**, 256–271 (2021).
745 2. Bechhofer, D. H. & Deutscher, M. P. Bacterial ribonucleases and their roles in RNA
746 metabolism. *Crit. Rev. Biochem. Mol. Biol.* **54**, 242–300 (2019).
747 3. Prossliner, T., Skovbo Winther, K., Sørensen, M. A. & Gerdes, K. Ribosome Hibernation.
748 *Annu. Rev. Genet.* **52**, 321–348 (2018).
749 4. Wada, A., Yamazaki, Y., Fujita, N. & Ishihama, A. Structure and probable genetic location
750 of a "ribosome modulation factor" associated with 100S ribosomes in stationary-phase
751 Escherichia coli cells. *Proc. Natl. Acad. Sci. U. S. A.* **87**, 2657–2661 (1990).
752 5. Prossliner, T., Gerdes, K., Sørensen, M. A. & Winther, K. S. Hibernation factors directly
753 block ribonucleases from entering the ribosome in response to starvation. *Nucleic Acids*
754 *Res.* **49**, 2226–2239 (2021).
755 6. Lipońska, A. & Yap, M.-N. F. Hibernation-Promoting Factor Sequesters Staphylococcus
756 aureus Ribosomes to Antagonize RNase R-Mediated Nucleolytic Degradation. *MBio* **12**,
757 e0033421 (2021).
758 7. Helena-Bueno, K. *et al.* A new family of bacterial ribosome hibernation factors. *Nature*
759 **626**, 1125–1132 (2024).
760 8. Van Dyke, N., Baby, J. & Van Dyke, M. W. Stm1p, a ribosome-associated protein, is
761 important for protein synthesis in Saccharomyces cerevisiae under nutritional stress
762 conditions. *J. Mol. Biol.* **358**, 1023–1031 (2006).
763 9. Wang, Y. J. *et al.* Lso2 is a conserved ribosome-bound protein required for translational
764 recovery in yeast. *PLoS Biol.* **16**, e2005903 (2018).
765 10. Leesch, F. *et al.* A molecular network of conserved factors keeps ribosomes dormant in the

766 egg. *Nature* **613**, 712–720 (2023).
767 11. McLaren, M. *et al.* CryoEM reveals that ribosomes in microsporidian spores are locked in
768 a dimeric hibernating state. *Nat Microbiol* **8**, 1834–1845 (2023).
769 12. Andersen, K. L. & Collins, K. Several RNase T2 enzymes function in induced tRNA and
770 rRNA turnover in the ciliate Tetrahymena. *Mol. Biol. Cell* **23**, 36–44 (2012).
771 13. Hillwig, M. S. *et al.* RNS2, a conserved member of the RNase T2 family, is necessary for
772 ribosomal RNA decay in plants. *Proc. Natl. Acad. Sci. U. S. A.* **108**, 1093–1098 (2011).
773 14. Haud, N. *et al. rnaset2* mutant zebrafish model familial cystic leukoencephalopathy and
774 reveal a role for RNase T2 in degrading ribosomal RNA. *Proceedings of the National*
775 *Academy of Sciences* **108**, 1099–1103 (2011).
776 15. Huang, H. *et al.* Bulk RNA degradation by nitrogen starvation-induced autophagy in yeast.
777 *EMBO J.* **34**, 154–168 (2015).
778 16. Minami, A. *et al.* The ribonuclease RNase T2 mediates selective autophagy of ribosomes
779 induced by starvation in Saccharomyces cerevisiae. *J. Biol. Chem.* 108554 (2025).
780 17. Sato, K. & Egami, F. STUDIES ON RIBONUCLEASES IN TAKADIASTASE. I. *J.*
781 *Biochem.* **44**, 753–767 (1957).
782 18. Luhtala, N. & Parker, R. T2 Family ribonucleases: ancient enzymes with diverse roles.
783 *Trends Biochem. Sci.* **35**, 253–259 (2010).
784 19. Spahr, P. F. & Hollingworth, B. R. Purification and Mechanism of Action of Ribonuclease
785 from Escherichia coli Ribosomes. *J. Biol. Chem.* **236**, 823–831 (1961).
786 20. Thompson, J. E., Venegas, F. D. & Raines, R. T. Energetics of catalysis by ribonucleases:
787 fate of the 2',3'-cyclic phosphodiester intermediate. *Biochemistry* **33**, 7408–7414 (1994).
788 21. Henneke, M. *et al.* RNASET2-deficient cystic leukoencephalopathy resembles congenital
789 cytomegalovirus brain infection. *Nat. Genet.* **41**, 773–775 (2009).
790 22. Greulich, W. *et al.* TLR8 Is a Sensor of RNase T2 Degradation Products. *Cell* **179**, 1264-
791 1275.e13 (2019).

792 23. Takayama, S. & Isogai, A. Self-incompatibility in plants. *Annu. Rev. Plant Biol.* **56**, 467–
793 489 (2005).
794 24. Beppu, T. & Arima, K. Induction by mercuric ion of extensive degradation of cellular
795 ribonucleic acid in Escherichia coli. *J. Bacteriol.* **98**, 888–897 (1969).
796 25. Meador, J., 3rd & Kennell, D. Cloning and sequencing the gene encoding Escherichia coli
797 ribonuclease I: exact physical mapping using the genome library. *Gene* **95**, 1–7 (1990).
798 26. Neu, H. C. & Heppel, L. A. THE RELEASE OF RIBONUCLEASE INTO THE MEDIUM
799 WHEN ESCHERICHIA COLI CELLS ARE CONVERTED TO SPEROPLASTS. *J. Biol.*
800 *Chem.* **239**, 3893–3900 (1964).
801 27. Datta, A. K. & Burma, D. P. Association of ribonuclease I with ribosomes and their
802 subunits. *J. Biol. Chem.* **247**, 6795–6801 (1972).
803 28. Kitahara, K. & Miyazaki, K. Specific inhibition of bacterial RNase T2 by helix 41 of 16S
804 ribosomal RNA. *Nat. Commun.* **2**, 1–7 (2011).
805 29. Fontaine, B. M. *et al.* RNase I regulates Escherichia coli 2',3'-cyclic nucleotide
806 monophosphate levels and biofilm formation. *Biochem. J* **475**, 1491–1506 (2018).
807 30. Flemming, H.-C. & Wuertz, S. Bacteria and archaea on Earth and their abundance in
808 biofilms. *Nat. Rev. Microbiol.* **17**, 247–260 (2019).
809 31. Ueta, M. *et al.* Ribosome binding proteins YhbH and YfiA have opposite functions during
810 100S formation in the stationary phase of Escherichia coli. *Genes Cells* **10**, 1103–1112
811 (2005).
812 32. Beckert, B. *et al.* Structure of a hibernating 100S ribosome reveals an inactive
813 conformation of the ribosomal protein S1. *Nature Microbiology* **3**, 1115–1121 (2018).
814 33. Dai, X. *et al.* Reduction of translating ribosomes enables Escherichia coli to maintain
815 elongation rates during slow growth. *Nat. Microbiol.* **2**, 16231 (2016).
816 34. Polikanov, Y. S., Blaha, G. M. & Steitz, T. A. How Hibernation Factors RMF, HPF, and
817 YfiA Turn Off Protein Synthesis. *Science* **336**, 915–918 (2012).

818 35. Kato, T. *et al.* Structure of the 100S ribosome in the hibernation stage revealed by electron
819 cryomicroscopy. *Structure* **18**, 719–724 (2010).
820 36. Rodriguez, S. M. *et al.* Nonspecific base recognition mediated by water bridges and
821 hydrophobic stacking in ribonuclease I from Escherichia coli. *Protein Sci.* **17**, 681–690
822 (2008).
823 37. Krissinel, E. & Henrick, K. Inference of macromolecular assemblies from crystalline state.
824 *J. Mol. Biol.* **372**, 774–797 (2007).
825 38. Jurrus, E. *et al.* Improvements to the APBS biomolecular solvation software suite. *Protein*
826 *Sci.* **27**, 112–128 (2018).
827 39. Seely, S. M. *et al.* Molecular basis of the pleiotropic effects by the antibiotic amikacin on
828 the ribosome. *Nat. Commun.* **14**, 4666 (2023).
829 40. Deutscher, Murray P. Chapter 9 Maturation and Degradation of Ribosomal RNA in
830 Bacteria. in *Progress in Molecular Biology and Translational Science* vol. 85 369–391
831 (Academic Press, 2009).
832 41. Chadani, Y. *et al.* Ribosome rescue by Escherichia coli ArfA (YhdL) in the absence of
833 trans-translation system. *Mol. Microbiol.* **78**, 796–808 (2010).
834 42. Fessler, M., Gummesson, B., Charbon, G., Svenningsen, S. L. & Sørensen, M. A. Short-
835 term kinetics of rRNA degradation in Escherichia coli upon starvation for carbon, amino
836 acid or phosphate. *Mol. Microbiol.* **113**, 951–963 (2020).
837 43. Saito, K. *et al.* Ribosome collisions induce mRNA cleavage and ribosome rescue in
838 bacteria. *Nature* **603**, 503–508 (2022).
839 44. Müller, C., Crowe-McAuliffe, C. & Wilson, D. N. Ribosome Rescue Pathways in Bacteria.
840 *Front. Microbiol.* **12**, 652980 (2021).
841 45. Garza-Sánchez, F., Gin, J. G. & Hayes, C. S. Amino acid starvation and colicin D
842 treatment induce A-site mRNA cleavage in Escherichia coli. *J. Mol. Biol.* **378**, 505–519
843 (2008).

844 46. Zhang, Y. *et al.* HflX is a ribosome-splitting factor rescuing stalled ribosomes under stress
845 conditions. *Nat. Struct. Mol. Biol.* **22**, 906–913 (2015).
846 47. Gao, H. *et al.* Study of the structural dynamics of the E coli 70S ribosome using real-space
847 refinement. *Cell* **113**, 789–801 (2003).
848 48. Mohan, S., Donohue, J. P. & Noller, H. F. Molecular mechanics of 30S subunit head
849 rotation. *Proc. Natl. Acad. Sci. U. S. A.* **111**, 13325–13330 (2014).
850 49. Yapici, I. *et al.* 4D Crystallography Captures Transient IF1-Ribosome Dynamics in
851 Translation Initiation. *bioRxiv* 2023.10.27.564398 (2023) doi:10.1101/2023.10.27.564398.
852 50. Shoji, S., Dambacher, C. M., Shajani, Z., Williamson, J. R. & Schultz, P. G. Systematic
853 chromosomal deletion of bacterial ribosomal protein genes. *J. Mol. Biol.* **413**, 751–761
854 (2011).
855 51. Akanuma, G. *et al.* Evolution of Ribosomal Protein S14 Demonstrated by the
856 Reconstruction of Chimeric Ribosomes in Bacillus subtilis. *J. Bacteriol.* **203**, (2021).
857 52. Xaplanteri, M. A., Papadopoulos, G., Leontiadou, F., Choli-Papadopoulou, T. & Kalpaxis,
858 D. L. The contribution of the zinc-finger motif to the function of Thermus thermophilus
859 ribosomal protein S14. *J. Mol. Biol.* **369**, 489–497 (2007).
860 53. Li, Y. *et al.* Zinc depletion induces ribosome hibernation in mycobacteria. *Proc. Natl.*
861 *Acad. Sci. U. S. A.* **115**, 8191–8196 (2018).
862 54. Dimitrova-Paternoga, L. *et al.* Structural basis of ribosomal 30S subunit degradation by
863 RNase R. *Nature* **626**, 1133–1140 (2024).
864 55. Baba, T. *et al.* Construction of Escherichia coli K-12 in-frame, single-gene knockout
865 mutants: the Keio collection. *Mol. Syst. Biol.* **2**, 2006.0008 (2006).
866 56. Dijk, J. & Littlechild, J. Purification of ribosomal proteins from Escherichia coli under
867 nondenaturing conditions. *Methods Enzymol.* **59**, 481–502 (1979).
868 57. Akiyama, N. *et al.* Structural insights into the decoding capability of isoleucine tRNAs
869 with lysidine and agmatidine. *Nat. Struct. Mol. Biol.* **31**, 817–825 (2024).

870 58. Vogel, H. J. & Bonner, D. M. ACETYLORNITHINASE OF ESCHERICHIA COLI:
871 PARTIAL PURIFICATION AND SOME PROPERTIES. *J. Biol. Chem.* **218**, 97–106
872 (1956).
873 59. O'Toole, G. A. Microtiter dish biofilm formation assay. *J. Vis. Exp.* (2011)
874 doi:10.3791/2437.
875 60. Minami, A. *et al.* Establishment of the improved colonization of Escherichia coli
876 laboratory strain in the intestine mediated by single gene deletion. *Biochem. Biophys. Res.*
877 *Commun.* 150448 (2024).
878 61. Shimizu, Y. *et al.* Cell-free translation reconstituted with purified components. *Nat.*
879 *Biotechnol.* **19**, 751–755 (2001).
880 62. Rivera, M. C., Maguire, B. & Lake, J. A. Dissociation of ribosomes into large and small
881 subunits. *Cold Spring Harb. Protoc.* **2015**, 363–367 (2015).
882 63. Zborníková, E., Knejzlík, Z., Hauryliuk, V., Krásný, L. & Rejman, D. Analysis of
883 nucleotide pools in bacteria using HPLC-MS in HILIC mode. *Talanta* **205**, 120161 (2019).
884 64. Bähre, H. & Kaever, V. Measurement of 2',3'-cyclic nucleotides by liquid
885 chromatography-tandem mass spectrometry in cells. *J. Chromatogr. B Analyt. Technol.*
886 *Biomed. Life Sci.* **964**, 208–211 (2014).
887 65. Mastronarde, D. N. Automated electron microscope tomography using robust prediction of
888 specimen movements. *J. Struct. Biol.* **152**, 36–51 (2005).
889 66. Punjani, A., Rubinstein, J. L., Fleet, D. J. & Brubaker, M. A. cryoSPARC: algorithms for
890 rapid unsupervised cryo-EM structure determination. *Nat. Methods* **14**, 290–296 (2017).
891 67. Pettersen, E. F. *et al.* UCSF ChimeraX: Structure visualization for researchers, educators,
892 and developers. *Protein Sci.* **30**, 70–82 (2021).
893 68. Yamashita, K., Palmer, C. M., Burnley, T. & Murshudov, G. N. Cryo-EM single-particle
894 structure refinement and map calculation using Servalcat. *Acta Crystallogr D Struct Biol*
895 **77**, 1282–1291 (2021).

69. Emsley, P., Lohkamp, B., Scott, W. G. & Cowtan, K. Features and development of Coot. *Acta Crystallogr. D Biol. Crystallogr.* **66**, 486–501 (2010).

70. Casañal, A., Lohkamp, B. & Emsley, P. Current developments in Coot for macromolecular model building of Electron Cryo-microscopy and Crystallographic Data. *Protein Sci.* **29**, 1069–1078 (2020).

71. Liebschner, D. *et al.* Macromolecular structure determination using X-rays, neutrons and electrons: recent developments in Phenix. *Acta Crystallogr D Struct Biol* **75**, 861–877 (2019).

72. Chen, V. B. *et al.* MolProbity: all-atom structure validation for macromolecular crystallography. *Acta Crystallogr. D Biol. Crystallogr.* **66**, 12–21 (2010).